



Preparation of Manganese Dioxide Supercapacitors by Secondary Construction of Three-Dimensional Substrates and Ion Embedding

Yihan Shi¹ · Ming Zhang¹ · Junshan Zhao¹ · Liu Zhang¹ · Xumei Cui¹ · Xinhua Zhu³ · Dandan Jin¹ · Jiali Gong¹ · Dingyu Yang¹ · Jitao Li²

Received: 6 April 2022 / Accepted: 12 June 2022 / Published online: 21 July 2022
© The Author(s) under exclusive licence to The Korean Institute of Metals and Materials 2022

Abstract

This work used a simple electrochemical reduction method to secondary construct the reduced nickel base (rNi Base) on nickel foam with a nano-core structure. The secondarily constructed base has a large specific surface area, which can increase the mass utilization of the active material. The rNi Base was used as a base for the reduction of nickel on Na^+ , K^+ , and NH_4^+ , respectively. MnO_2 was electrodeposited under three different cation pre-intercalation treatments, and the mechanism of the effect of different monovalent cations to guide the growth of MnO_2 materials was investigated. Finally, rNi/ MnO_2 & Na^+ electrode with a special nano cauliflower structure was obtained. The special nanostructure of the electrode enhances its electrochemical performance, possessing 598 F g^{-1} ultra-high specific capacitance at a current density of 1 A g^{-1} and a high specific capacitance of 307.5 F g^{-1} at a high current density of 20 A g^{-1} , and high specific capacitance maintenance rate of 92.7% after 500 cycles of charging and discharging at a current density of 2 A g^{-1} . In addition, the symmetrical supercapacitor assembled with this electrode has a very high specific capacitance (401.1 F g^{-1} at a current density of 1 A g^{-1}) and energy density (80.22 Wh kg^{-1} at a power density of 599.99 W kg^{-1}).

✉ Dingyu Yang
yangdingyu@cuit.edu.cn

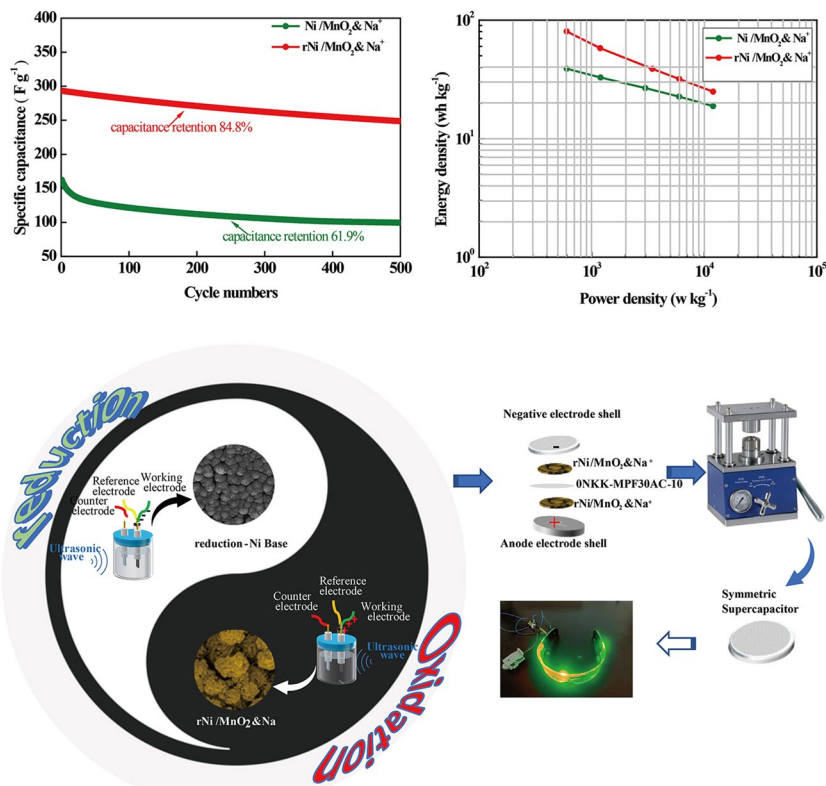
✉ Jitao Li
jtlee@tju.edu.cn

² School of Precision Instruments and Optoelectronics Engineering, Tianjin University, 300072 Tianjin, China

³ College of Intelligent Manufacturing, Sichuan University of Arts and Science, 635000 Dazhou, China

¹ College of Optoelectronic Engineering, Chengdu University of Information Technology, 610225 Chengdu, China

Graphical Abstract



Keywords MnO_2 · Symmetric supercapacitor · Nano cauliflower

1 Introduction

The problems of energy shortage and environmental pollution in the 21st century have stimulated the desire for clean and renewable energy [1, 2]. In order to effectively alleviate the problem of unstable wind and solar power generation, energy storage technology is facing unprecedented challenges [3]. As a new type of energy storage element between conventional capacitors and chemical batteries, it is widely used in portable electronic devices, electric vehicles, etc. [3, 4]. Supercapacitors have the advantages of high discharge power, large electric capacity at Farad level, high energy, wide operating temperature range and extremely long service life, maintenance-free, economic and environmental protection, etc., and have received more and more attention in recent years [5–7]. Supercapacitors have double-layer capacitance and Faraday pseudocapacitance two energy storage mechanisms. The former mainly generates stored energy by adsorption of pure electrostatic charges on the electrode surface; the latter mainly generates Faraday pseudocapacitance by rapidly reversible redox reactions on and near the surface of the electrode

material, resulting in higher energy density [8–11]. Electrode materials are the core components that affect the performance of supercapacitors. Transition metal oxides are widely used as electrode materials for supercapacitors [12–15]. Among many types of transition metal oxides, manganese oxide MnO_2 is considered the most promising next-generation supercapacitor electrode material with abundant reserves, low cost, non-toxic and non-polluting, and high theoretical specific capacity (1370 F g^{-1}) [16–18].

The electrodeposition method has many advantages over the conventional methods of MnO_2 preparation. First, Faraday reactions mainly occur at the electrode surface and inside the shallow bulk phase not exceeding 500 nm [19], so in order to approach the theoretical specific capacitance of MnO_2 , the MnO_2 film thickness should tend to be infinitesimal, which can accelerate electron and electrolyte ion transport and ensure that the MnO_2 active material is fully applied to energy storage [20]. The use of electrochemical methods for deposition of MnO_2 electrodes can well control the film thickness and increase the material mass utilization as much as possible, which in

turn improves the electrode specific capacitance. Secondly, the preparation of MnO₂ electrode materials by electrochemical methods does not require the introduction of conductive agents or binders, which avoids the introduction of excess mass to reduce the specific capacitance of the material [21]. Unique designed materials are benefit for improving the properties the prepared materials [22–26]. In the preparation process of MnO₂ electrode materials with the electrodeposition method, different combinations of manganese oxygen octahedral [MnO₆] units can form various crystalline forms, including α , β , γ , λ and various morphologies, including nanoparticles, nanowires, nanosheets, and nanoflowers, in which different morphologies correspond to different specific surface areas as well as ion migration paths, thus exhibiting different electrochemical properties [27–31]. Moreover, the electrodeposition method can grow nanomaterials directly from conductive three-dimensional porous skeletal materials as a base to obtain electrodes with high surface area and hierarchical structure. Additionally, with electrodeposition method, the three-dimensional porous scaffolds with high conductivity can be used as the substrate-based nanoparticles for growth, thus obtaining electrodes with high surface area and hierarchical structure. The three-dimensional porous scaffolds with high conductivity can not only provide sufficient binding sites for the loading electroactive material, thus alleviating the shedding of active materials due to volume changes of the electrodes during the charge/discharge cycle, but also accelerate insertion and desorption of electrolyte ions on the electrode/electrolyte interface, improving the surface reaction rate [25]. Lang prepared a 100 nm thick nanoporous gold film that facilitated ion diffusion between MnO₂ and electrolyte and provided bilayer capacitance [32]. Zhang used self-assembled opal as a template to electrodeposit nickel to obtain a bicontinuous electrode, and the removal of the template resulted in a nickel-inverse opal (with a porosity of about 74%), which prevents the electrolytic active material from conformal deep into the structure discontinuous ion paths generated by deposition, thus improving the charge/discharge rate [32]. However, the scarcity of precious metals and the tedious preparation process limit the application of both in large quantities, respectively.

In this work, we report a simple method to secondary construct refined three-dimensional nickel foam bases with a large specific surface area, which increases the mass utilization of the active material, and the high conductivity network of this structure, which facilitates the transport of electrons and electrolyte ions. The three-dimensional nickel foam as a base was electrically reduced in NiSO₄ that mixed solution to construct a nickel foam on reduced nickel base (rNi Base) with a nano-core structure. Subsequently, rNi Base was used as a base to electrodeposit MnO₂ under three different

monovalent cation pre-intercalation treatment conditions of Na⁺, K⁺, NH₄⁺, and finally rNi/MnO₂&Na⁺ electrode with special nano cauliflower structure was obtained. This electrode has an excellent performance in supercapacitors.

2 Experiment

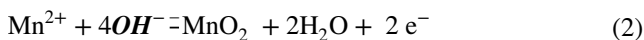
2.1 Preparation of Electrode

First, the three-dimensional porous foam Ni base (3*2 cm²) was placed into dilute hydrochloric acid, deionized water, and anhydrous ethanol for 15 min of ultrasonic cleaning to remove nickel oxides and oil stains on the surface of the nickel base, and the electrooxidation of anhydrous ethanol can guide the rapid and uniform deposition of the active material, which makes the film thickness more uniform and controllable and the utilization of the active material higher [34, 35]. Subsequently, the reduced nickel base (rNi Base) on nickel foam was obtained in an ultrasonic-assisted three-electrode system (France BioLogic electrochemical workstation, nickel foam as the working electrode, saturated Ag/AgCl as the reference electrode, and Pt electrode as the counter electrode) by using an electrochemical reduction method with 0.06 mol L⁻¹ NiSO₄, Na₂SO₄ (200 mL, AR, CHRON CHEMICALS) mixed solution as the precursor solution, the deposition voltage and deposition time were -1 V and 100 s, respectively. The reactions occurring during the preparation of rNi Base by electroreduction are shown in Eq. (1).



Then the two groups of bases (Ni base, rNi Base, rZn Base) were ultrasonically cleaned in deionized water and put into a vacuum drying oven for drying, and the masses of the bases were weighed and recorded after drying. Subsequently, each base was used as a working electrode in a three-electrode system with ultrasonic assistance in precursor solutions containing three different cations of Na⁺, K⁺, NH₄⁺ (0.06 mol L⁻¹ MnSO₄, Na₂SO₄ mixed solution, 0.06 mol L⁻¹ MnSO₄, K₂SO₄ mixed solution, 0.06 mol L⁻¹ MnSO₄, (NH₄)₂SO₄ mixed solution) were pre-intercalated and electrodeposited to obtain six sets of electrode samples (Ni/MnO₂&Na⁺, Ni/MnO₂&K⁺, Ni/MnO₂&NH₄⁺; rNi/MnO₂&Na⁺, rNi/MnO₂&K⁺, rNi/MnO₂&NH₄⁺). The MnSO₄, Na₂SO₄, K₂SO₄, (NH₄)₂SO₄ we used were purchased from CHRON CHEMICALS Company, and the purity was analytical grade (AR). The introduction of ultrasonic oscillation during the deposition process can effectively reduce the concentration polarization caused by the rapid consumption of metal ions at the electrode attachment, making the deposition more uniform [34], the deposition

process occurs with the reaction as follows (2)[36], The deposit, on process is shown in Fig. 1.



The samples were dried and weighed. The mass difference between the two weighing results was the mass of the active material of the electrode sheet, as shown in Table 1.

Table 1 Active material quality of sample electrodes

Electrode	Quality(mg)
Ni/MnO ₂ & Na ⁺	1.7
Ni/MnO ₂ & K ⁺	1.5
Ni/MnO ₂ & NH ₄ ⁺	1.3
rNi/MnO ₂ & Na ⁺	1.3
rNi/MnO ₂ & K ⁺	1.1
rNi/MnO ₂ & NH ₄ ⁺	1.0

Each electrode sheet was directly stamped into a 14 mm electrode sheet using a punching machine, and the two stamped electrode sheets were used as the positive and negative electrodes, ONKK-MPF30AC-10 as the diaphragm, 1 mol L⁻¹ Na₂SO₄ solution as the electrolyte, and CR2016 type battery cases as the positive and negative cases for the assembly of each symmetrical capacitor. Figure 2 exemplifies the preparation process of rNi/MnO₂ & Na⁺ symmetrical capacitors.

2.2 Material Morphology Characterization

The surface morphology and microstructure of each base and electrode were observed by scanning electron microscopy (SEM, Zeiss ULTRA 55 SEM), and the transmission electron microscopy (TEM, FEI Tecnai G2 F20) was used to observe the fine structures of the rNi/MnO₂ & Na⁺, and the XPS technique was used to determine the rNi/MnO₂ & Na⁺ elemental valence distribution on the surface.

Fig. 1 The deposition process of rNi/MnO₂ & Na⁺

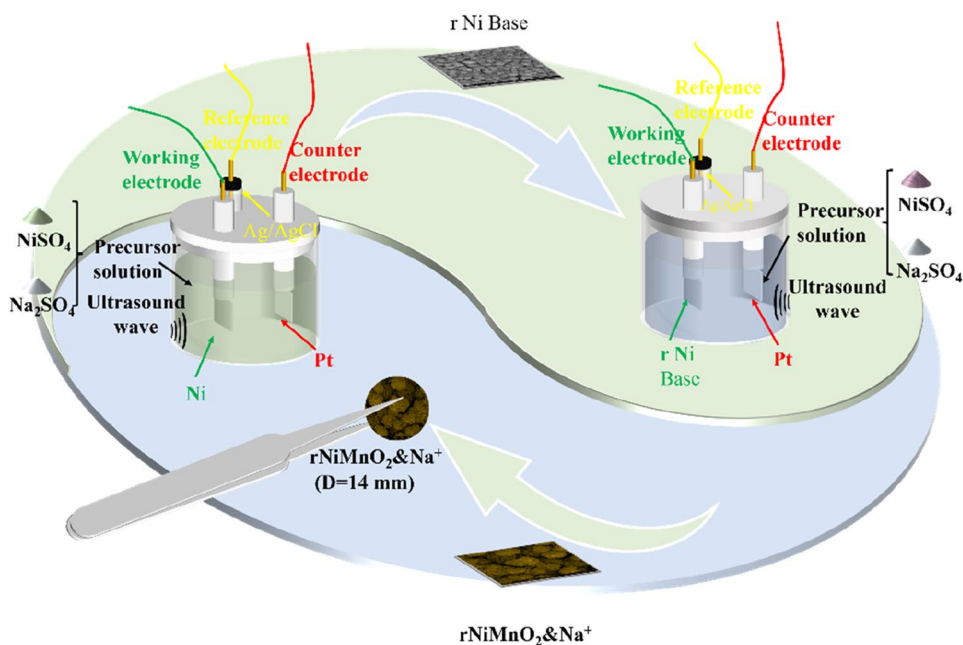
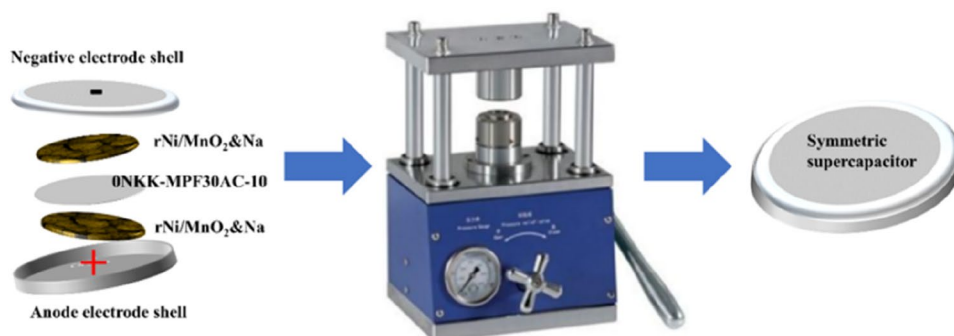


Fig. 2 Preparation process of symmetric supercapacitor



2.3 Electrode Electrochemical Performance Test

The electrode electrochemical performance tests were performed through chronoamperometry (CA), cyclic voltammetry (CV) in a three-electrode system (each MnO_2 electrode as the working electrode, Ag/AgCl as the reference electrode, and Pt electrode as the counter electrode) on a French BioLogic electrochemical workstation by using $1 \text{ mol L}^{-1} \text{ Na}_2\text{SO}_4$ solution as the electrolyte. According to the galvanostatic charge/discharge curve and cyclic voltammetry curve, which were obtained from the test, the following Eqs. (3) and (4) were applied to calculate the materials' mass-specific capacity C_m and area-specific capacity C_s , respectively [37, 38].

$$C_m = \frac{Q}{V \cdot m} = \frac{I_g \Delta t}{\Delta V \cdot m} \quad (3)$$

In Eq. (3), I_g represents the mass current density for charging and discharging, Δ represents the charging and discharging time, m represents the mass of the MnO_2 electrode sheet, and Δ represents the voltage change of complete charging and discharging.

$$C_s = \frac{\int IdV}{s \Delta v V} \quad (4)$$

In Eq. (4), s represents the area of the MnO_2 electrode sheet, Δv represents the scan rate, V represents the scan interval, and \int represents half of the area of CV curve integral.

2.4 Symmetric Supercapacitor Electrochemical Performance Test

The assembled symmetrical supercapacitors were rested for 12 h, French Biologic electrochemical workstation was used for AC impedance testing of symmetrical supercapacitors, with a frequency range from 0.01 Hz to 100 kHz and an amplitude of 5 mV. The device was then under cyclic voltammetric testing with a scan rate of 5 mV-s⁻¹ to determine the voltage window of each device for constant current charging and discharging Testing. According to the constant current charge and discharge curve of the supercapacitor and formula (3), the mass-specific capacitance C_m of the device can be calculated, then the following two formulas (5) and (6) can be used to calculate the energy density of the electrode under different current densities (E) (Wh kg^{-1}) and power density (P) (W kg^{-1}) [37].

$$E = \frac{C_m \Delta V^2}{2 \times 3.6} \quad (5)$$

$$P = \frac{E}{\Delta t} \times 3600 \quad (6)$$

where ΔV represents the voltage window during charging and discharging, and Δt represents the device discharge time.

3 Result and Analysis

3.1 SEM and TEM Analysis

In order to systematically investigate the mechanism of the role played by the electrode material base and cation pre-intercalation in the growth process of MnO_2 nanomaterials, scanning electron microscopy (SEM) was used to observe the samples and bases. Figure 3 shows the SEM photographs of each base and electrode material. First, it is observed that the rNi base constructed after electrochemical reduction treatment shows a nano-core structure compared to the normal Ni base. Moreover, the base morphology has a significant influence on the deposition process of the electrode material, and the growth of MnO_2 nanomaterials shows a staggered nanorod structure in the normal Ni Base, while the secondary constructed rNi Base shows a nano cauliflower structure formed by fine nanospheres encapsulated on the surface of the irregular core base. As shown in Fig. 4, on the one hand, because the surface of the irregular core structure of rNi Base provides more active sites for the growth of MnO_2 , the bond between the MnO_2 film growing on the sites and the base is tighter and less likely to fall off, which can enhance the electrode cycling performance. On the other hand, due to the unevenness of the irregular core-shell structure of rNi Base, the core-shell protrusions are more likely to accumulate charges, guiding the growth of MnO_2 nanorods for spherical structure aggregation.

In addition, the electrode morphology obtained from the deposition of different species of cations after pre-intercalation treatment is quite different, which is related to the ionic radius of the cation and the transport capacity [39]. Compared with Na^+ and NH_4^+ , K^+ has a larger ionic radius, and its transport capacity is also lower. Hence, the MnO_2 deposited by K^+ pre-intercalation on each base is not as uniform as that deposited by Na^+ and NH_4^+ pre-intercalation, and the electrodes deposited by NH_4^+ pre-intercalation shows a tip aggregation effect of growth, which is attributed to the low ionic radius of NH_4^+ , and the high conductivity synergistically makes it easier to transport aggregation to the negative electrode resulting in the concentration of power lines. Compared with Ni/ MnO_2 & NH_4^+ electrode deposited on a normal base (Ni Base) after NH_4^+ pre-intercalation treatment, the Ni/ MnO_2 & NH_4^+ electrode deposited on rNi Base exhibits a rime structure due to the interaction between the

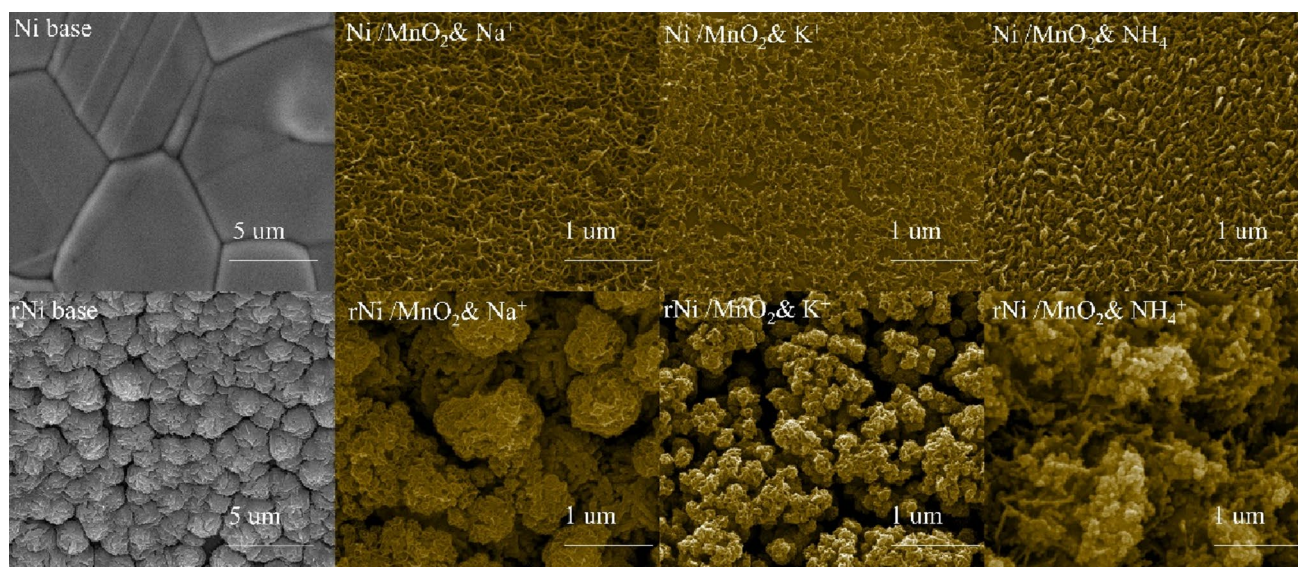


Fig. 3 SEM pictures of base and electrodes

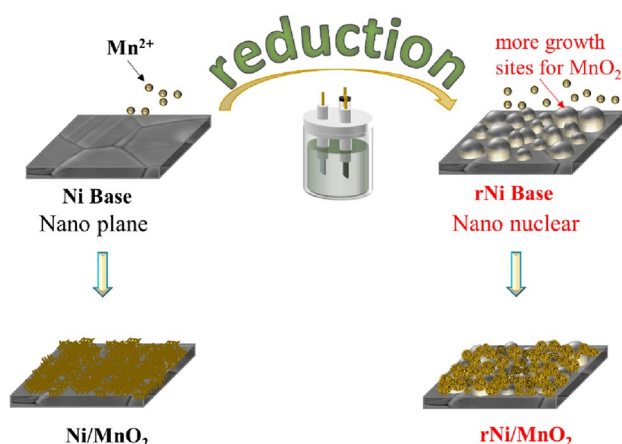


Fig. 4 rNi/MnO₂ growth mechanism diagram

surface microscopic morphology of rNi Base and rNi Base and the tip effect caused by NH₄⁺.

In order to further determine the microstructure of the electrodes, transmission electron microscopy (TEM) was used to observe Ni/MnO₂&Na⁺, and electron diffraction (SAED), element mapping, and high resolution-transmission electron microscopy (HR-TEM) analyses were performed. The results are shown in Fig. 5. Combined with the results in Fig. 5a, a nano-embroidered ball structure of MnO₂ nanomaterials uniformly wrapped on the surface of Ni core can be observed on the rNi/MnO₂&Na⁺ surface, and this structure as a unit constitutes the nano cauliflower structure in the SEM photo, which is beneficial to provide more Faraday redox reaction sites. Figure 5c, d shows the HR-TEM photographs of rNi/MnO₂&Na⁺ electrodes, where the lattice

stripes of the material can be observed with crystal plane spacing of $d_1 = 0.172$ nm, $d_2 = 0.202$ nm, $d_3 = 0.206$ nm, and $d_4 = 0.226$ nm, corresponding to the (501), (202), (401), and (002) crystal planes of MnO₂, respectively [40]. In addition, the results of element mapping show that Mn, O, and Na are uniformly distributed on the Ni element surface, which further indicates that the MnO₂ material is encapsulated on the Ni core surface while confirming the successful pre-insertion of Na⁺ into the rNi/MnO₂ electrode.

3.2 XPS Analysis

To further investigate the oxidation state and chemical composition of the sample surface, rNi/MnO₂&Na⁺ were determined by X-ray photoelectron spectroscopy technique, and the results are shown in Fig. 6.

Figure 6b shows the Ni2p spectrum of rNi/MnO₂&Na⁺ electrode. Due to the multiple splitting property of Ni, there are 10 characteristic peaks, which can be divided into three groups of peaks, Ni Metal, NiO, and Ni(OH)₂ in general. Among them, 852.5 eV, 871.3 eV are the 2p_{3/2} and 2p_{1/2} peaks of Ni Metal, respectively [41, 42], 854.0 eV, 860.7 eV, 873.1 eV, 878.9 eV are the 2p_{3/2}, 2p_{3/2} satellite, 2p_{1/2}, 2p_{3/2} satellite peaks of NiO, respectively [43–45], 855.8 eV, 862.5 eV, 876.2 eV, 881.1 eV are the 2p_{3/2}, 2p_{3/2} satellite, 2p_{1/2}, 2p_{3/2} satellite peaks of Ni(OH)₂, respectively [45]. Figure 6(c) shows the Mn2p spectrum of rNi/MnO₂&Na⁺ electrode with two characteristic peaks at 653.2 eV and 641.4 eV with a spin energy interval of 11.8 eV corresponding to Mn³⁺ [46, 47], 640.4 eV is the Auger generated from Ni base [44], and 645 eV is the peak of MnSO₄[48]. The spectrum of O1s in Fig. 6d can be divided into two peaks. The peak at

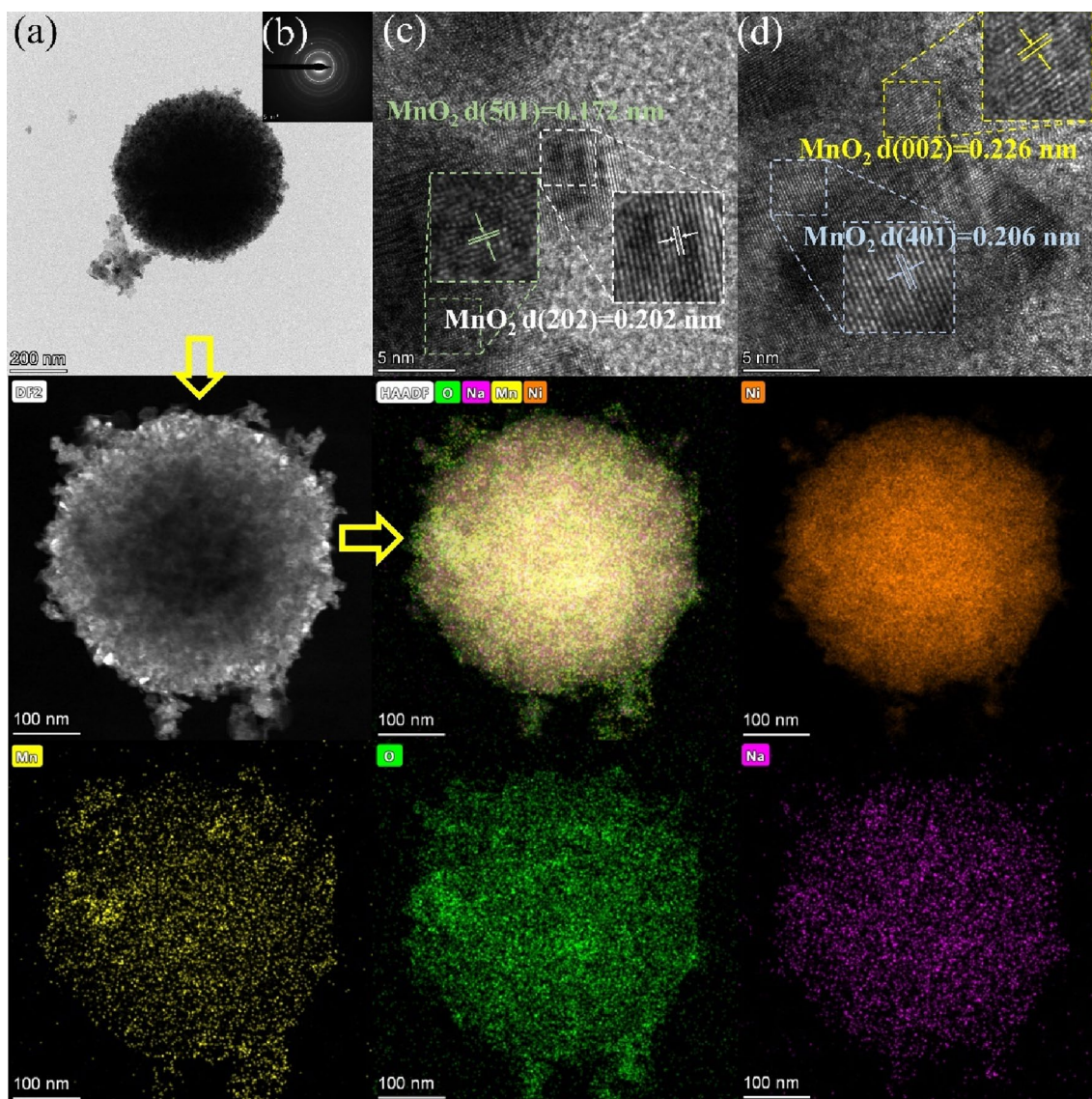


Fig. 5 TEM, HR-TEM, TEM mapping photos of rNi/MnO₂&Na⁺ electrode

529.5 eV can be attributed to its association with Mn-O-Mn, Ni-O [49, 50], while the other peak at 531.2 eV corresponds to C=O, which may be caused by CO₂ in the air. The presence of one peak in the high-resolution Na1s spectrum is a characteristic peak of Na₂SO₄, which can be further combined with TEM elemental mapping to indicate the smooth pre-insertion of Na⁺ into the rNi/MnO₂ electrode.

3.3 The Electrode Electrochemical Performance

The electrochemical properties of the prepared sample electrodes were tested by the constant current charge/discharge method and linear cyclic voltammetry. The reaction equation during electrochemical charging and discharging can be expressed by Eq. (7) [51, 52].



Figure 7a shows the curve of electrodeposition preparation of electrodes, and it can be seen that the values of current in the deposition decreased as the resistance increased due to the generation of MnO₂. The electrodeposition process is carried out with the help of ultrasonic vibration, which leads to a small jitter of the deposition current. Figure 7b–d display the constant current charge/discharge curves of each electrode at current density of 1, 2 and 5 A g⁻¹ respectively. (e) shows the constant current charge/discharge curve of rNi/MnO₂ & NH₄⁺ at the current density of 10 and 20 A g⁻¹ respectively. First, it can be observed that the GCD curve of the electrodes deposited on rNi Base was more similar to the form of an equilateral triangle, compared

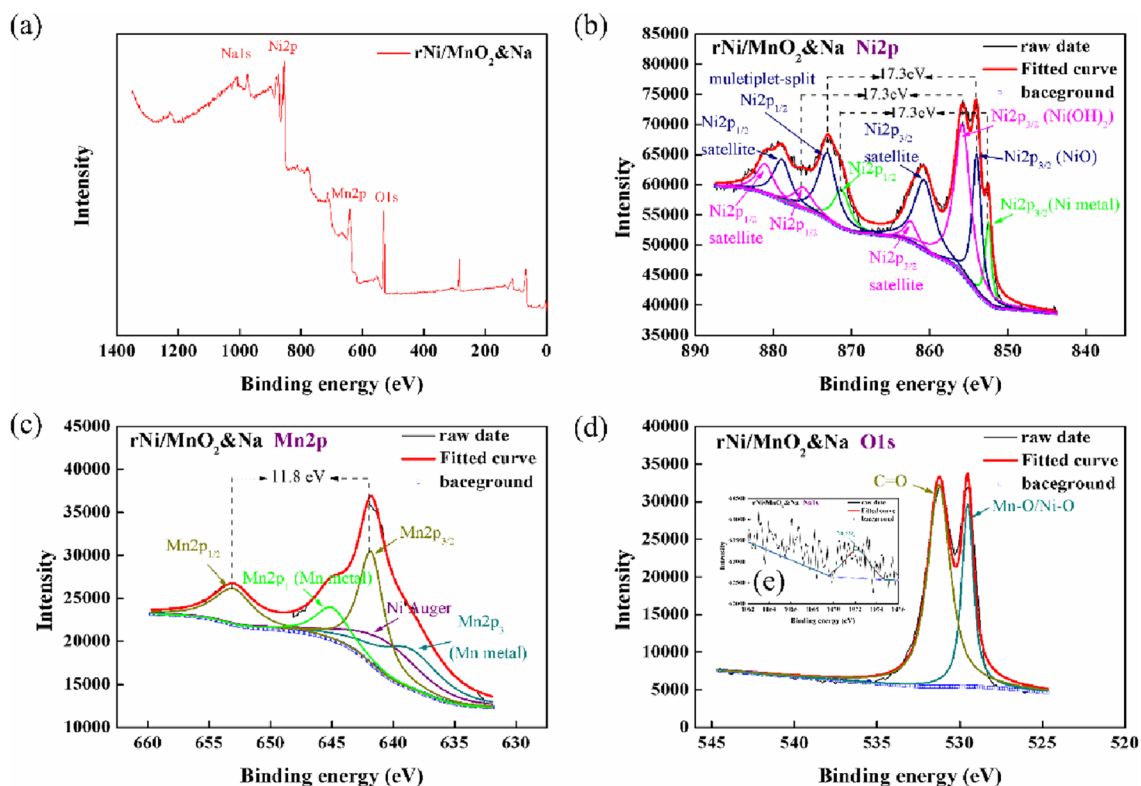


Fig. 6 a XPS survey spectra of rNi/MnO₂&Na⁺ b Mn 2p XPS spectra of rNi/MnO₂&Na⁺, c O 1s XPS spectra of rNi/MnO₂&Na⁺ d S 2p XPS spectra spectra of rNi/MnO₂&Na⁺, e C 1s XPS spectra of rNi/MnO₂&Na⁺, f C 1s XPS spectra of rNi/MnO₂&Na⁺

to those normal electrodes deposited on rNi Base deposited, indicating that they have highly reversible redox reactions [39], significantly longer discharging times and lower IR drop, which can be attributed to the larger specific surface area of the electrodes deposited on the core-shell structure of rNi Base. The high specific surface area morphology not only provides more redox reaction sites, thus increasing the electrode pseudocapacitance, but also possesses a smaller resistivity, which reduces the electrode series equivalent resistance (ESR) and ultimately results in a lower IR drop [53, 54].

Secondly, the electrodes deposited after the construction of ion channels by different cation pre-intercalation layers exhibit different charging and discharging properties, which are closely related to the surface structure of the electrode materials. Due to the tip effect played by the synergistic effect of the low ionic radius and high mobility of NH₄⁺, NH₄⁺ guides the MnO₂ growth to be more uniform and flatter, conferring a lower resistance to the electrode. However, when NH₄⁺ guided MnO₂ was deposited on the rNi Base, the uneven core-shell structure of the base exacerbated the tip aggregation effect of NH₄⁺, forming a rime structure of the rNi/MnO₂ & NH₄⁺ electrode. Moreover, the Faraday redox reaction occurs mainly near the electrode surface. The rime structure of this electrode has a larger film thickness, leading

to the coverage of most of the active material and low porosity reduction mass utilization between MnO₂, which ultimately makes the electrodeless specific capacitance. It is worth mentioning that the GCD curves of rNi/MnO₂&Na⁺ exhibit the longest discharge time among all the electrodes, which is attributed to the unique three-dimensional nano-cauliflower structure of this electrode. The high specific surface area and high porosity of this structure can provide more Na⁺ embedding and de-embedding sites, and the mass utilization of active material is improved, which makes this electrode possess ultra-high specific capacitance at current densities of 1, 2, 5, 10, 20 A⁻¹ current densities of 598, 484.6, 402.2, 349.2, and 307.5 F g⁻¹, respectively. (see Table 2 for comparison with previous studies). The high specific capacity and good discharging performance of the electrode are attributed to its microporous nano-cauliflower structure, which has open spaces between the single nanorods that make up the nanospheres to facilitate electrolyte penetration into the inner regions of the electrode. Also, the high specific surface area and overlapping nanowire structure can shorten ion oxidation and electron diffusion pathways and provide more active sites for electrochemical reactions. [55, 56]

Cyclic voltammetry is a critical means to examine the performance of electrode materials, as shown in Fig. 7g–i. First, the appearance of a set of symmetrical redox peaks in

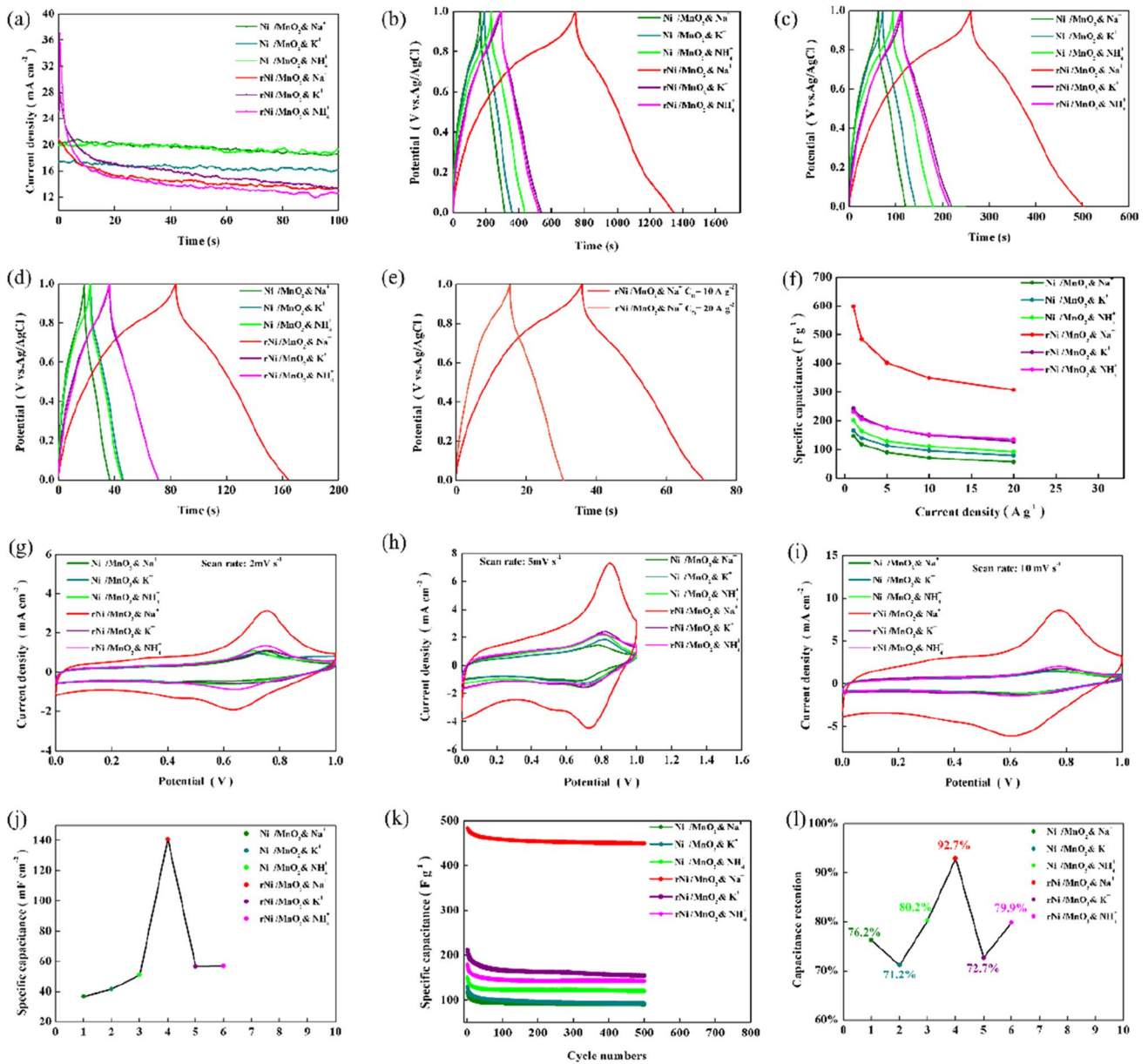


Fig. 7 **a** shows the current time curves of electrode deposition preparation. **b**, **c** and **d** present constant current charge/discharge curve(s) for each electrode at current density of 1, 2, 5, 1.2, and 5 A g⁻¹ respectively. **e** displays high current charge/discharge curves of rNi/MnO₂&Na⁺. **f** shows the mass-specific capacity of each electrode. **g**,

h and **i** present CV curves of each electrode at different voltage scan rates. **j** displays the area-specific capacity of each electrode at a current density of 5 mV s⁻¹. **k** shows the long-term cycling performance of each electrode at a current density of 2 A g⁻¹. **l** presents capacitance retention of each electrode at a current density of 2 A g⁻¹

Table 2 Comparison of electrode specific capacity

Specific capacitance	Current density	Electrode	Reference
347 F ⁻¹	1 A g ⁻¹	MnO ₂ /RGO	[60]
292 F ⁻¹	1 A g ⁻¹	3D-MnO ₂ /Ni	[61]
426.4 F ⁻¹	0.5 A g ⁻¹	MO25	[62]
598 F ⁻¹	1 A g ⁻¹	rNi/MnO ₂ & Na ⁺	Our work

the interval between 0.6 and 0.9 on a rectangular shape CV curve is typical capacitive behavior of MnO₂. The energy storage is contributed by the surface adsorption/desorption of electrolyte cations (H⁺, Na⁺) on the nickel foam network and MnO₂, and the insertion of Na⁺ into MnO₂ from the electrolyte through reversible redox reactions [57, 58]. With the increasing sweep rate, the area capacity decreased, which was caused by a late reaction. All samples have a pair of distinct redox peaks at around 0.6–0.9 V. Moreover, compared

to the electrodes deposited on a normal base, the absolute value of the ratio of the redox peak magnitudes was closer to 1 for the electrodes deposited on two secondary constructed bases of rNi Base, which indicates a more reversible redox reaction for this electrode [49]. The area ratio capacitance of each electrode was derived from the CV test results combined with Eq. (4), as shown in Fig. 7j. The area-specific capacitance of the rNi/MnO₂&Na⁺ samples is the highest among the groups, reaching 141 mF cm⁻², thanks to the ultra-high specific surface area nano-cauliflower structure. The cycling performance of each electrode was obtained by the GCD method with a current density of 2 A g⁻¹ in 1 mol L⁻¹ Na₂SO₄ for 500 cycles of charge and discharge (Fig. 7k, l). The decrease of capacitance performance in the initial phase is mainly due to the dissolution of manganese dioxide in Na₂SO₄ solution. In fact, during the test phase, we also observed that the sodium sulfate solution turned brown. Thanks to the structural stability of rNi/MnO₂&Na⁺, MnO₂ has more contact with the base and is more viscous, thus obtaining high cycle retention rates of 92.7%. Furthermore, we can conclude that the electrodes exhibit a battery-type capacitive behavior based on the characteristics of the CD and CV curves. Because the concept of Farad (abbreviated F) did not apply to the pure behavior of Faraday rotation

[59], we supplemented the mass-specific capacity of the electrodes. The specific capacities of rNi/MnO₂&Na⁺ electrodes at current density of 1, 2, 5, 10, and 20 A g⁻¹, were 166.1, 134.6, 111.7, 97.0 and 85.4 mAh g⁻¹, respectively.

Electrochemical impedance is one of the crucial means to study the reaction kinetics and mechanism of supercapacitor electrode materials. The electrochemical reaction process of the electrode is shown in Fig. 8a, which can be divided into the Faraday process and the double-layer capacitance process, where the Faraday process can be further divided into charge transfer and concentration polarization resulting in the material transfer process, and produce charge

Table 3 The values of R_{ct} and R_Ω for sample electrodes

Electrode	R _{ct} (Ω)	R _Ω (Ω)
Ni/MnO ₂ & Na ⁺	1.25	0.83
Ni/MnO ₂ & K ⁺	1.44	0.97
Ni/MnO ₂ & NH ₄ ⁺	1.14	0.87
rNi/MnO ₂ & Na ⁺	1.08	0.83
rNi/MnO ₂ & K ⁺	1.16	0.82
rNi/MnO ₂ & NH ₄ ⁺	1.15	0.85

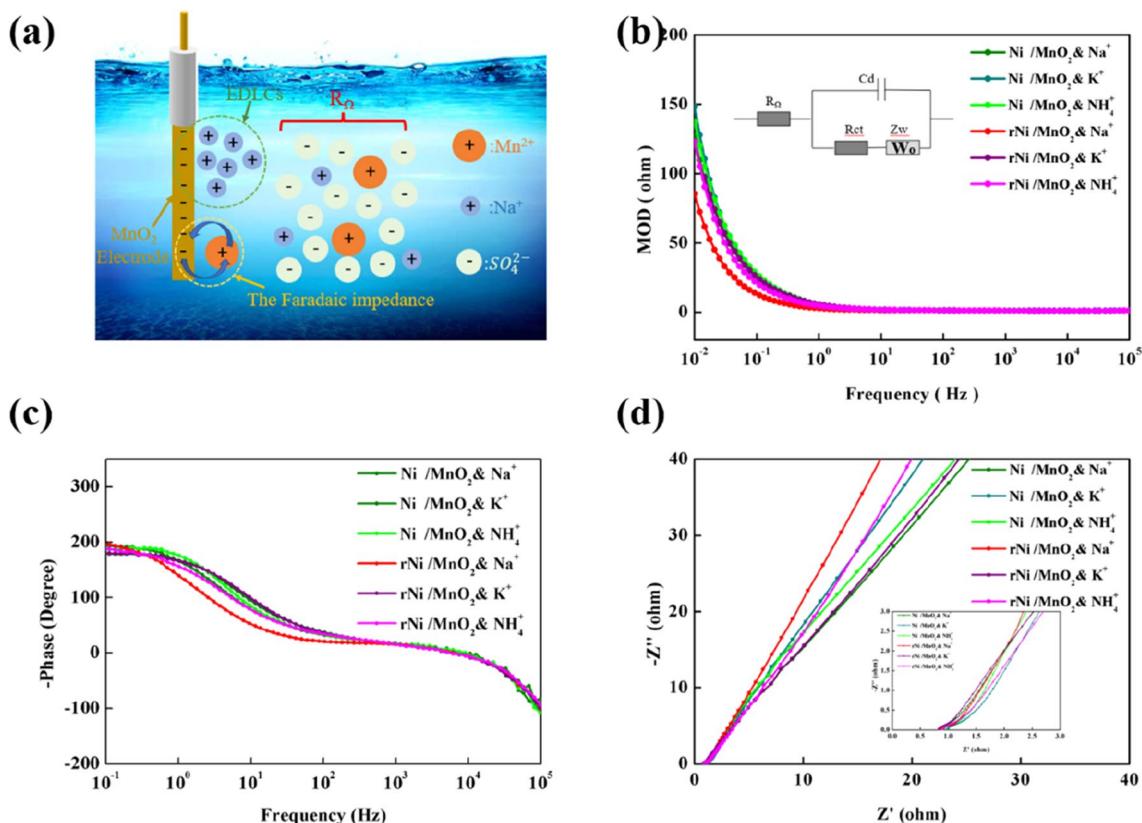


Fig. 8 **a** The electrode electrochemical reaction process, **b** The fitting circuit and the variation of impedance modulus with frequency, **c** Bode plot of each MnO₂ film electrode, **d** Nyquist plot of each MnO₂ film electrode

transfer resistance R_{ct} and Warburg impedance Z_w , respectively. The overall reaction process of the electrode can be abstractly represented as the equivalent circuit shown in Fig. 8b (where R_{Ω} is the resistance between the electrode material and the electrolyte, C is the double layer capacitance, and Z_f is the Faraday impedance due to the redox reaction, $Z_f = R_{ct} + Z_w$). Figure 8c shows the Bode diagram of each MnO_2 film electrode, and the impedance decreases with increasing frequency, reflecting the capacitive characteristics of the electrode. In the Bode phase angle diagram of the supercapacitor in the ideal state, the phase angle in the low-frequency region is supposed to be close to 90° and the phase angle in the high-frequency region is supposed to be close to 0° . The phase angle deviating from the ideal capacitor in the low-frequency region is 90° , which is thought to be related to the porous structure of the film [63]. According to Fig. 8(d), the impedance modulus of each electrode decreases with increasing frequency and is even only about 2Ω in the high-frequency region, which exhibits a typical capacitive behavior. In the high-frequency range, the electrode reaction kinetics is mainly controlled by the charge transfer process, and the impedance spectrum exhibits a semicircle with an intercept of R_{Ω} on the semicircle and the real axis, and the diameter of the circle is the charge transfer resistance (R_{ct}) [64]. It resembles a straight line in the low-frequency range and corresponds to the Warburg (Z_w) impedance of the reactants diffusing from the solution to the electrode reaction interface [65].

Based on the results of the Nyquist plot, we performed a component fit to obtain the values of R_{ct} and R_{Ω} (shown in Table 3). $rNi/MnO_2 \& Na^+$ has a lower R_{ct} and R_{Ω} , which is attributed to the high specific surface area of the electrodes and is consistent with the SEM analysis.

4 Symmetric Supercapacitor Electrochemical Performance

The performance of the symmetrical supercapacitor assembled with $Ni/MnO_2 \& Na^+$ and $rNi/MnO_2 \& Na^+$ electrodes is shown in Fig. 9. Figure 9a shows the cyclic voltammetry

curves of each symmetrical device. First, it can be seen that the symmetrical device composed of electrodes deposited on rNi Base obtains a larger CV curve area for the same cation pre-intercalation treatment, which indicates that the area specific capacitance of the device is improved. It can be attributed to the high specific surface area of the electrodes with the nano-cauliflower indicated morphology. Secondly, each electrode has a pair of redox peaks in the $-0.2-1$ V voltage interval, so we performed the devices in the $-0.2-1$ V voltage interval with 1, 2, 5, 10, 20 $A g^{-1}$, and obtained the GCD curves and rate performance of the two devices, as shown in Fig. 9b, c, respectively. $rNi/MnO_2 \& Na^+$ symmetrical devices possess ultra-high specific capacities of 401.1, 289.9, 194, 159.1, and 124.5 $F g^{-1}$ at 1, 2, 5, 10, and 20 $A g^{-1}$ current densities.

The power density (P) and energy density (E) are also critical electrochemical properties of supercapacitors, and the results are calculated from the GCD curves using Eqs. (6), (7) are shown in Fig. 9d. The $rNi/MnO_2 \& Na^+$ capacitor has a higher energy density ($80.22 Wh kg^{-1}$ at $599.99 W kg^{-1}$ power density). Even at a high power density of $11997.98 W kg^{-1}$ the energy density can reach $24.90 Wh kg^{-1}$. The cycling performance of each device shown in Fig. 9e was obtained by charging and discharging at a constant current density of $2 A g^{-1}$ for 500 times. The overall performance was similar to the electrode cycling performance test, and the decrease in capacitance performance of the same device at the initial stage was mainly due to the dissolution of MnO_2 in the Na_2SO_4 electrolyte. The symmetrical supercapacitor composed of $rNi/MnO_2 \& Na^+$ as electrodes benefits from the high specific surface area of rNi base, more contact between MnO_2 material and base, which improves the adhesion strength of MnO_2 , and at the same time, the structural stability is stronger, and high cycle retention rate of 84.8% is obtained. Using the same three $rNi/MnO_2 \& Na^+$ symmetrical supercapacitors in series as the power supply driver, an LED lamp with a rated voltage of 3 V was successfully lit, as shown in Fig. 9f.

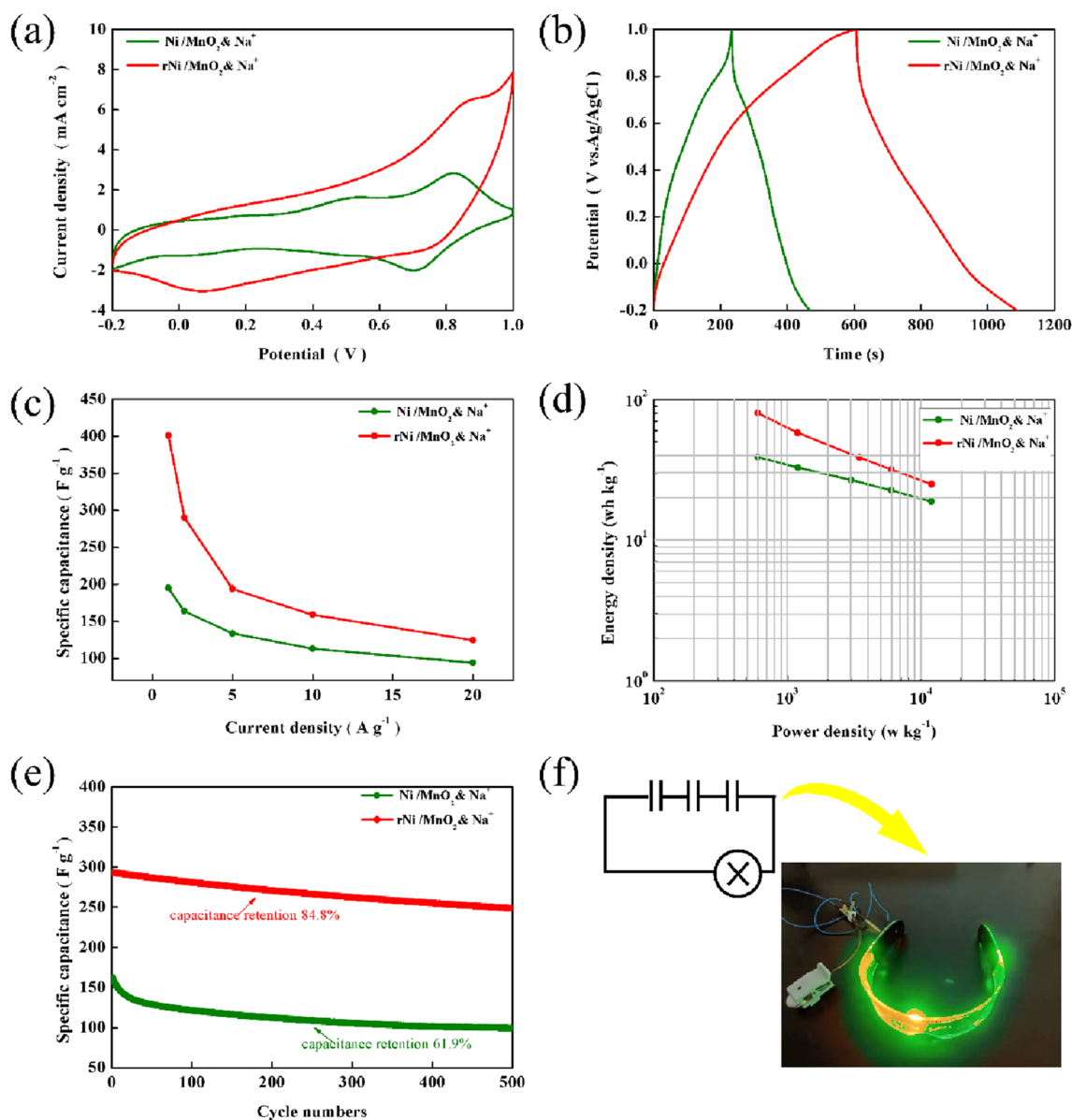


Fig. 9 **a.** the cyclic voltammetry curves of symmetrical devices, **b.** GCD curves devices, **c.** rate performance of the two devices, **d.** power density (P) and energy density (E) of supercapacitors, **e.** The cycling

performance of devices, **f** Three $rNi/MnO_2 \& Na^+$ symmetrical devices are connected in series to light the 3V LED lamp

5 Conclusions

In summary, a simple electrochemical reduction method was used to secondary construct the reduced nickel base (rNi Base) on nickel foam with a nano-core structure, and the secondary constructed base has a large specific surface area, which can increase the mass utilization of the active material. MnO_2 was electrodeposited under three different monovalent cation pre-intercalation treatments of Na^+ , K^+ , and NH_4^+ using rNi Base as the base, and the mechanism of action of different cations guiding the growth of MnO_2

materials was investigated. SEM and TEM results show that the $rNi/MnO_2 \& Na^+$ electrode obtained by electro-deposition on rNi Base after pre-intercalation of Na^+ has a special nano-cauliflower structure. Moreover, the electrode has a high specific capacitance (598 F g^{-1} at a current density of 1 A g^{-1}), low solution resistance (1.08Ω) and charge transfer resistance (0.82Ω), even at a high current density of 20 A g^{-1} at high current densities, the specific capacitance is still as high as 3307.5 F g^{-1} , and after 500 cycles of charging and discharging at a current density of 2 A g^{-1} , the specific capacitance maintenance rate is as high as 92.7%. In addition, the symmetrical

supercapacitor assembled with this electrode has a very high specific capacitance (401.1 F g^{-1} at a current density of 1 A g^{-1}) and energy density (80.22 Wh kg^{-1} at a power density of 599.99 W kg^{-1}), even at a high power density of $11997.98 \text{ W kg}^{-1}$, the energy density can reach 24.90 Wh kg^{-1} .

Acknowledgements The current work was financed by National Natural Science Foundation of China (NSFC) No. 11675029 and 51708015 and supported by Sichuan Science and Technology Program (2021JDRC0020).

Data Availability The data that support the findings of this study are available from the corresponding author upon reasonable request.

Declarations

Conflict of interest The authors declare no conflict of interest.

References

- Subramanian, V., Zhu, H.W., Vajtai, R., Ajayan, P.M.: Hydrothermal synthesis and pseudocapacitance properties of MnO_2 nanostructures. *J. Phys. Chem. B*. **109**, 20207–20214 (2005)
- Guo, Y.G., Hu, J.S., Wan, L.J.: Nanostructured Materials for Electrochemical Energy Conversion and Storage Devices. *Adv. Mater.* **20**, 2878–2887 (2008)
- Miller, J.M.: Energy storage system technology challenges facing strong hybrid, plug-in and battery electric vehicles. In: *Vehicle Power and Propulsion Conference*. pp. 4–10. (2009)
- Adhyapak, P.V., naddanimath, T., Pethkar, S., Chandwadkar, A.J., Negil, Y.S., Vijayamohan, K.: Application of electrochemically prepared carbon nanofibers in supercapacitors. *J. Power Sources*. **109**, 105–110 (2002)
- Simon, P., Gogotsi, Y., Dunn, B.: Where Do Batteries End and Supercapacitors Begin. *Science*. **343**, 1210–1211 (2014)
- Simon, P., Gogotsi, Y.: Materials for electrochemical capacitors. *Nat. Mater.* **7**, 845–854 (2008)
- Miller, J.R., Simon, P.: Materials science. electrochemical capacitors for energy management. *Science*. **321**, 651–652 (2008)
- Liu, S.B., Zhao, Y., Zhang, B.H., Xia, H., Zhou, J.F., Xie, W.K., Li, H.J.: Nano-micro carbon spheres anchored on porous carbon derived from dual-biomass as high rate performance supercapacitor electrodes. *J. Power Sources*. **381**, 116–126 (2018)
- Babakhani, B., Lvey, D.G.: Anodic deposition of manganese oxide electrodes with rod-like structures for application as electrochemical capacitors. *J. Power Sources*. **195**, 2110–2117 (2010)
- Wang, H., Hu, Y.J., Fan, J.C., Zhang, Y.H., Zhang, Q.C.: Collision Detection Based on Bounding Box for NC machining Simulation. *Phys. Procedia*. **24**, 247–252 (2012)
- Wei, W.F., Cui, X.W., Chen, W.X., Lvey, D.G.: Manganese oxide-based materials as electrochemical supercapacitor electrodes. *Chem. Soc. Rev.* **40**, 1697–1721 (2011)
- Yongpeng, M., Xiubo, X., Wenyue, Y., Zhipeng, Y., Xueqin, S., Yuping, Z., Xiaoyang, Y., Hideo, K., Chuanxin, H., Zhanhu, G., Wei, D.: Recent advances in transition metal oxides with different dimensions as electrodes for high-performance supercapacitors. *Adv. Compos. Hybrid. Mater.* **4**, 906–924 (2021)
- Wei, D., Xiaoning, W., Jie, Z., Xueqin, S., Litao, K., Fuyi, J., Xiaoyu, Z., Qian, S., Mengyao, D., Hu, L., Vignesh, M.: Zhanhu G. Biological cell template synthesis of nitrogen-doped porous hollow carbon spheres/ MnO_2 composites for high-performance asymmetric supercapacitors. *Electrochim. Acta*. **296**, 907–915 (2019)
- Wu, D., Yu, H., Hou, C., Xinhui, S., Tiansha, S., Xueqin, S., Bing, W.: NiS nanoparticles assembled on biological cell walls-derived porous hollow carbon spheres as a novel battery-type electrode for hybrid supercapacitor. *J. Mater. Sci.* **55**, 14431–14446 (2020)
- Dan, W., Xiubo, X., Yongpeng, M., Jingjing, Z., Chuanxin, H., Xueqin, S., Xiaoyang, Y., Yuping, Z., Hideo, K.: Wei D. Morphology controlled hierarchical NiS/carbon hexahedrons derived from nitrilotriacetic acid-assembly strategy for high-performance hybrid supercapacitors. *Chem. Eng. J.* **433**, 133673 (2022)
- Xu, C.J., Kang, F.W., Li, B.H., Du, H.: D. Recent progress on manganese dioxide based supercapacitors. *J. Mater. Res.* **25**, 1421–1432 (2010)
- Toupin, M., Brousse, T., Bélanger, D.: Influence of microstructure on the Charge Storage Properties of Chemically Synthesized Manganese Dioxide. *C Chem. Mater.* **14**, 3946–3952 (2002)
- Li, M., Chen, Q., Zhan, H.: Ultrathin manganese dioxide nanosheets grown on partially unzipped nitrogen-doped carbon nanotubes for high-performance asymmetric supercapacitors. *J. Alloy Compd.* **702**, 236–243 (2017)
- Toupin, M., Brousse, T., Belanger, D.: Charge storage mechanism of MnO_2 electrode used in aqueous electrochemical capacitor. *Chem. Mater.* **16**, 3184–3190 (2004)
- Xiao, J.W., Yang, S.X., Fei, L.W., Wang, X.S.: Electrodeposition of manganese oxide nanosheets on a continuous three-dimensional nickel porous scaffold for high performance electrochemical capacitors. *J. Power Sources*. **245**, 1027–1034 (2014)
- Guillemet, P., Brousse, T., Crosnier,.; Dandeville, Y., Athouel, L.: Scudeller, Y. modeling pseudo capacitance of manganese dioxide. *Electrochim. Acta*. **67**, 41–49 (2012)
- Yongliang, L., Hua, Y., Yanbing, C., Xiaoyu, W., Kunyan, S., Ye qiang, T.: Application and exploration of nanofibrous strategy in electrode design. *J. Mater. Sci. Technol.* **74**, 189–202 (2021)
- Yankun, Z., Zhen, Y., Wenxin, F., Yunchao, W., Guangzhen Li, Hailin, C., Hua, Y.: Carbon nanotube/carbon fiber electrodes via chemical vapor deposition for simultaneous determination of ascorbic acid, dopamine and uric acid. *Arab. J. Chem.* **13**, 3266–3275 (2020)
- Zhanpo, H., Xiaoyan, Z., Hua, Y., Zhende, L., Guangzhen, L., Huayu, Z., Ye qiang, T.: Graphene oxide/gold nanoparticle/graphite fiber microelectrodes for directing electron transfer of glucose oxidase and glucose detection. *J. Power Sourc.* **521**, 230956 (2022)
- Li, G., Hua, Y., Jinjin, M., Enhao, D., Huayu, Z., Zhende, L., Yankun, Z., Yifeng, D.: Xiaoyan Z. Electrochemical detection of nitrate with carbon nanofibers and copper co-modified carbon fiber electrodes. *Compos. Commun.* **29**, 101043 (2022)
- Yanbing, C., YuxiaoW.; Zhen, L., Dandan, W., Hua, Y., Hongzhang, Z.: Ye qiang T. A flame retarded polymer-based composite solid electrolyte improved by natural polysaccharides. *Compos. Commun.* **26**, 100774 (2021)
- Kazemi, S.H., naghmi, M.G.: Kiani, n. A. Electrodeposited manganese dioxide nanostructures on electro-etched carbon fibers: high performance materials for supercapacitor applications. *Mater. Res. Bull.* **60**, 137–142 (2014)
- Xue, T., Xu, C.L., Zhao, D.D., Li, X.H., Li, H.L.: Electrodeposition of mesoporous manganese dioxide supercapacitor electrodes through self-assembled triblock. *J. Power Sources*. **164**, 953–958 (2007)
- Ye, Z.G., Li, T., Ma, G., Peng, X.Y., Zhao: J. morphology controlled MnO_2 electrodeposited on carbon fiber paper for high-performance supercapacitors. *J. Power Sources*. **351**, 51–57 (2017)

30. Zhang, Y., Wang, B., Liu, F., Cheng, J., Zhang, X.W., Zhang, L.: Full synergistic contribution of electrodeposited three-dimensional NiCo₂O₄@MnO₂ nanosheet networks electrode for asymmetric supercapacitors. *Nano. Energy*. **27**, 627–637 (2016)
31. Purushothaman, S., Jeyasubramanian, K., Muthuselvi, M., Hikku, G.S.: Cu₂O nanosheets decorated CuMnO₂ nanosphere electrodeposited on Cu foil as high-performance supercapacitor electrode. *Mat. Sci. Semicon. Proc.* **121**, (2021)
32. Lang, X.Y., Hirata, A., Fujita, T., Chen, M.W.: Nanoporous metal/oxide hybrid electrodes for electrochemical supercapacitors. *Nat. Nanotechnol.* **6**, 232–236 (2011)
33. Zhang, H.G., Yu, X.D., Braun, P.V.: Three-dimensional bicontinuous ultrafast-charge and discharge bulk battery electrodes. *Nat. Nanotechnol.* **6**, 277–281 (2011)
34. Zhang, M., Yang, D.Y., Li, J.T.: Ultrasonic and NH₄⁺ assisted Ni foam base oxidation to achieve high performance MnO₂ supercapacitor. *Appl. Surf. Sci.* **541**, 148546 (2021)
35. Zhang, M., Yang, D.Y., Li, J.T.: Effective improvement of electrochemical performance of electrodeposited MnO₂ and MnO₂/reduced graphene oxide supercapacitor materials by alcohol pretreatment. *J. Energy Storage*. **30**, 101511 (2020)
36. Zhang, M., Chen, Y.: Dingyu Yang.; Jitao Li. High performance MnO₂ supercapacitor material prepared by modified electrodeposition method with different electrodeposition voltages. *J. Energy Storage*. **29**, 101363 (2020)
37. Yang, W., He, L., Tian, X., Yan, M., Yuan, H., Liao, X., Meng, J., Hao, Z., Mai, L.: Carbon-MEMS-based alternating stacked MoS₂@rGO-CNT micro-supercapacitor with high capacitance and energy density. *Small*. **13**, 1–8 (2017)
38. Wei, C., Xu, Q., Chen, Z., Rao, W., Fan, L., Yuan, Y., Bai, Z.: Xu. An all-solstate yarn supercapacitor using cotton yarn electrodes coated with polypyrrole nanotubes. *Carbohydr. Polym.* **169**, 50–57 (2017)
39. Feng, M., Du, Q., Su, L., Zhang, G., Wang, G., Ma, Z., Gao, W., Qin, X., Shao, G.: Manganese oxide electrode with excellent electrochemical performance for sodium ion batteries by preintercalation of K and Na ions. *Sci. Rep-uk*. **7**, 2219 (2017)
40. Li, H., Wang, W.L., Pan, F., Xin, X., Chang, Q., Liu, X.: Synthesis of single-crystalline α -MnO₂ nanotubes and structural characterization by HRTEM. *Mat. Sci. Eng. B-adv.* **176**, 10541057 (2011)
41. Powell, C.J.: Recommended Auger parameters for 42 elemental solids. *J. Electron. Spectrosc.* **185**, 1–3 (2012)
42. Colpas, G.J., naroney, M.J., Bagyinka, C., Kumar, Willis, W.S., Suib, S.L., nascharak, P.K.: Baidya, N. X-ray spectroscopic studies of nickel complexes, with application to the structure of nickel sites in hydrogenases. *Inorg. Chem.* **30**, 920–928 (1991)
43. Klein, J.C., Hercules, D.M.: Surface characterization of model Urushibara catalysts. *J. Catal.* **82**, 424–441 (1983)
44. Lian, K., Thorpe, S.J., Kirk, D.W.: Electrochemical and surface characterization of electrocatalytically active amorphous NiCo alloys. *Electrochim. Acta*. **37**, 2029–2041 (1992)
45. Mansour, A.: Characterization of LiNiO₂ by XPS. *Surf. Sci. Spectra*. **3**, 279–286 (1994)
46. Xie, A., Wang, H., Zhu, Z., Zhang, W., Li, X., Wang, Q., Luo, S.: mesoporous CeO₂- α -MnO₂-reduced graphene oxide composite with ultra-high stability as a novel electrode material for supercapacitor. *Surf. Interface*. **25**, 101177 (2021)
47. Allen, G.C., Harris, S.J., Jutson, J.A., Dyke, J.M.: A study of a number of mixed transition metal oxide spinels using X-ray photoelectron spectroscopy. *Appl. Surf. Sci.* **37**, 111–134 (1988)
48. Nesbitt, H.W., Banerjee, D.: Interpretation of XPS Mn(2p) spectra of Mn oxyhydroxides and constraints on the mechanism of MnO₂ precipitation. *Am. Mineral.* **83**, 305–315 (1998)
49. Strohmeier, B.R., Hercules, D.M.: Surface Spectroscopic Characterization of Manganese/Aluminum oxide Catalysts. *J. Phys. Chem.* **88**, 4922–4929 (1984)
50. Löchel, B.P., Strehblow, H.H.: Breakdown of Passivity of Nickel by Fluoride. *J. Electrochem. Soc.* **131**, 713 (1984)
51. Zhang, Q., Levi, M.D., Dou, Q.: The charge storage mechanisms of 2D cation-intercalated manganese oxide in different electrolytes. *Adv. Energy Mater.* **8**, 1–10 (2018)
52. Cao, J., Li, X., Wang, Y., Walsh, F.C., Ouyang, J.H., Jia, D., Zhou, Y.: Materials and fabrication of electrode scaffolds for deposition of MnO₂ and their true performance in supercapacitors. *J. Power Sources*. **293**, 657–674 (2015)
53. SiXu Deng, D., Wu, S.C.H., Wang, H., JingBing, L.: YuXiu Suna, Hui Yan. Synthesis and electrochemical properties of MnO₂ nanorods/graphene composites for supercapacitor applications. *Elect. Act.* **111**, 707–712 (2013)
54. Xiangcang, R.E.N., Chuanjin, T.I.A.N., Sa, L.I., Yucheng, Z.H.A.O., Chang-An, W.A.N.G.: Facile synthesis of tremella-like MnO₂ and its application as supercapacitor electrodes. *Front. Mater. Sci. Chin.* **3**, 234–240 (2015)
55. Xu, C.L., Zhao, Y.Q., Yang, G.W., Li, F.S.: Li. Mesoporous nanowire array architecture of manganese dioxide for electrochemical capacitor applications. *Chem. Commun.* **48**, 7575 (2009)
56. Jiang, H., Zhao, T., Ma, J., Yan, C.Y., Li, C.Z.: Ultrafine manganese dioxide nanowire network for high-performance supercapacitors. *Chem. Commun.* **47**, 1264 (2011)
57. Li, X.-B., Xu, G.-R.: Hydrothermal vs electrodeposition: how does deposition method affect the electrochemical capacitor performance of manganese dioxide? *Ceram. Int.* **43**, 8963 (2017)
58. K ping Wang, Teng, H.: Structural feature and double-layer capacitive performance of porous carbon powder derived from polyacrylonitrile-based carbon fiber. *J. Electrochem. Soc.* **154**, A993 (2007)
59. Thierry Brousse, D., Belanger, J.W.: Long. To Be or Not To Be Pseudocapacitive? *J. Electrochem. Soc.* **162**, A5185–A5189 (2015)
60. Zhang, M., Yang, D.Y., Li, J.T.: Supercapacitor performances of MnO₂ and MnO₂/reduced graphene oxide prepared with various electrodeposition times. *Vacuum*. **178**, 109455 (2020)
61. Mahdi, F., Javanbakht, Shahrokhian, S.: Anodic pulse electrodeposition of mesoporous manganese dioxide nanostructures for high performance supercapacitors. *J. Alloy Compd.* **887**, 161376 (2021)
62. Swain, N., nitra, A., Saravanakumar, B., Balasingam, S.K., Ramadoss, A.: Construction of Three-Dimensional MnO₂/Ni Network as an Efficient Electrode material for High Performance Supercapacitors. *Electrochim. Acta.* **342**, 136041 (2020)
63. Stoller, M.D., Park, S., Zhu, Y., An, J., Ruoff, R.S.: Graphene-based ultracapacitors. *Nano Lett.* **8**, 3498 (2008)
64. Wang, K.P., Teng, H.S.: Structural feature and double-layer capacitive performance of porous carbon powder derived from polyacrylonitrile. *J. Electrochem. Soc.* **154**, A993–A998 (2007)
65. Stoller, M.D., Park, S.J., Zhu, Y.W., An, J., Ruoff, R.S.: Graphene-based ultracapacitors. *Nano Lett.* **8**, 3498–3502 (2008)

Publisher's Note Springer Nature remains neutral with regard to jurisdictional claims in published maps and institutional affiliations.